applied optics

Adaptive filter design via a gradient thresholding algorithm for compressive spectral imaging

Nelson Diaz,[1] Hoover Rueda,[2] and Henry Arguello[3,*]

[1]Department of Electrical Engineering, Universidad Industrial de Santander, Bucaramanga 680002, Colombia
[2]Department of Electrical and Computer Engineering, University of Delaware, Delaware 19716, USA
[3]Department of Computer Science, Universidad Industrial de Santander, Bucaramanga 680002, Colombia
*Corresponding author: henarfu@uis.edu.co

Received 24 January 2018; revised 4 May 2018; accepted 7 May 2018; posted 8 May 2018 (Doc. ID 320542); published 8 June 2018

Sensing a spectral image data cube has traditionally been a time-consuming task since it requires a scanning process. In contrast, compressive spectral imaging (CSI) has attracted widespread interest since it requires fewer samples than scanning systems to acquire the data cube, thus improving the sensing speed. CSI captures linear projections of the scene, and then a reconstruction algorithm estimates the underlying scene. One notable CSI architecture is the color coded aperture snapshot spectral imager (C-CASSI), which employs pixelated filter arrays as the coding patterns to spatially and spectrally encode the incoming light. Up to date works on C-CASSI have used non-adaptive color coded apertures. Non-adaptive sampling ignores prior information about the signal to design the coding patterns. Therefore, this work proposes a method to adaptively design the color coded aperture, such that the quality of image reconstruction is improved. In more detail, this work introduces a gradient thresholding algorithm, which computes the consecutive color coded aperture from a rapidly reconstructed low-resolution version of the data cube. The successive adaptive patterns enable recovering a data cube in the presence of Gaussian noise with higher image quality. Real reconstructions and simulations evidence an improvement of up to 3 dB in the quality of image reconstruction of the proposed method in comparison with state-of-the-art non-adaptive techniques.

OCIS codes: (110.4234) Multispectral and hyperspectral imaging; (110.1085) Adaptive imaging; (170.1630) Coded aperture imaging; (110.1758) Computational imaging.

https://doi.org/10.1364/AO.57.004890

1. INTRODUCTION

Spectral imaging (SI) collects 3D spatiospectral information of a scene, referred to as data cube, with two spatial dimensions and one spectral dimension. Each spatial position along the spectral axis is known as a spectral signature, which can be used to determine the components present in the scene. SI has attracted widespread interest due to the numerous applications, for example, in cultural heritage for noninvasive characterization and identification of the deterioration state of materials [1], in medicine for the diagnosis of oral cancer [2], and in food safety to detect pathogens [3]. Traditionally, SI systems rely on scanning techniques to collect the data cube [4,5]. For instance, push-broom is a line-scanning methodology that moves across a spatial dimension to construct the data cube; by concatenating 2D spatio-spectral slices, whisk-broom is a point-scanning method that moves across the two spatial dimensions capturing each spectrum at a time; and the tunable spectral filter is a wavelength-scanning methodology that constructs the data cube by capturing each spectral band at a time. Collecting a data cube using conventional scanning techniques is a time-consuming effort, non-suitable for dynamic varying targets. In contrast, snapshot systems are faster than scanning systems because they capture all the information about the scene at once. One of the first snapshot architectures is the computer tomography imaging spectrometer (CTIS), which is composed of a slit spectrometer, a kinoform grating, and a detector array. When the linear dispersive element is replaced by a 2D disperser, it is possible to capture projections from different angles. Therefore, tomography techniques are used to build an SI. CTIS is a compact architecture, but its major disadvantage is the difficulty in manufacturing the kinoform dispersing elements [6]. Another snapshot architecture is multispectral beam splitting (MSBS), which splits the light into different color bands by means of a tandem of beam splitters, with the intensity being registered in different sensors. This system, however, is limited to five or six spectral bands due to difficulties in dividing the beam or successive losses when several filters are used [7]. A third widely used architecture is the snapshot hyperspectral imaging Fourier transform spectrometer (SHIFT), based on two birefringent Normarski prisms behind

an $N \times M$ lenslet array, forming $N \times M$ sub-images in the detector array. SHIFT is easy to fabricate, but it is affected by the parallax effect [8]. Lastly, one of the most recent snapshots architectures is coded aperture snapshot spectral imaging (CASSI), which is considered to be the first spectral imager based on compressive sensing (CS) [9].

CASSI is a snapshot system that captures compressive projections of the data cube and then exploits CS theory concepts to estimate the data cube [9–13]. In their cutting-edge paper published in 2006, Candes, Tao, and Donoho demonstrate that it is possible to recover an s-sparse n-dimensional signal from $s\log(n)$ randomly chosen projections. For that reason, the number of compressive measurements of CASSI are fewer than that of conventional snapshot architectures. The main elements in CASSI are the coded aperture, the dispersive element, and the detector. In CASSI, the incoming light of the scene is spatially modulated by the coded aperture and spectrally smeared by the dispersive element. The modulated and smeared intensity is then multiplexed in the focal plane array (FPA) forming the compressive measurements. Traditionally, CASSI uses a block-unblock coded aperture that blocks or transmits the whole spectral signature in a given pixel. Recently, the color-patterned CASSI system (C-CASSI) gained much attention due to its flexibility to filter the incoming light per pixel [14–16] with the use of a color coded aperture (CCA). A CCA is a 2D pixelated filter, which not only encodes the scene spatially, but also spectrally. In comparison with block-unblock coded apertures, CCA permits the selection of portion of the spectrum that enters into the system. A CCA can be understood as a 3D block-unblock coded aperture, where each slice of the 3D coding patterns represents the filtering applied to each spectral band. Figure 1 shows the equivalence between a 3D block-unblock coded aperture and the color coded aperture. Each spectral filter is represented by a vector of block-unblock elements, and the size of the vector denotes the spectral resolution. Conventional C-CASSI uses low-pass, bandpass, and high-pass filters to modulate the incoming light.

On the other hand, up-to-date work on C-CASSI has focused on non-adaptive measurements [14,15]. With adaptive measurements, we refer to the use of prior knowledge of the data cube in the design of the entries of the CCA. Specifically, during the capturing of K snapshots, the compressive measurements $\mathbf{y}^0, \mathbf{y}^1, \cdots, \mathbf{y}^{K-1}$ are sequentially captured according to the structure of the scene, but capturing $\mathbf{y}^{\ell+1}$ depends on the previously gathered measurements $\mathbf{y}^{\ell}$. Adaptive sensing has been used in the past in areas such as high-dynamic-range imaging to improve the quantization resolution and to avoid saturation [17]. Between the adaptive methodologies in SI there are three different approaches. The first approach is based on dictionary learning [18], which consists of learning a dictionary from the data, then computing a singular value decomposition from the dictionary, and finally using a small number of left singular vectors as the measurement matrix $\mathbf{H}$. The reconstruction is then performed with a conventional CS signal recovery method. Adaptive sampling using dictionary learning performs better than conventional CS methods according to Ref. [18]. The adaptive sampling in the wavelet domain developed by Averbuch *et al.* [19] shows that it is possible to sample the wavelet coefficients with a digital micromirror device (DMD) for the single pixel architecture. This method acquires low-resolution measurements, and then, based on the previous measurements and using the properties of the wavelet structure, the algorithm adaptively extracts the significant information corresponding to the edges of the image. Adaptive sampling based on the Bayes method relies on the inversion of the compressive measurements $\mathbf{y} = \mathbf{H}\boldsymbol{\Psi}^{-1}\boldsymbol{\theta} + \boldsymbol{\omega}$ from a Bayesian perspective. The prior belief is based on the idea that $\boldsymbol{\theta}$ is of the signal a sparse representation in some basis $\boldsymbol{\Psi}$. The objective is to provide a posterior belief of the entries of $\boldsymbol{\theta}$ [20]. Specifically, Bayesian compressive sensing estimates the prior information of the covariance matrix from the measurement matrix and compressive measurements. Using that knowledge, the next sensing matrix is inferred.

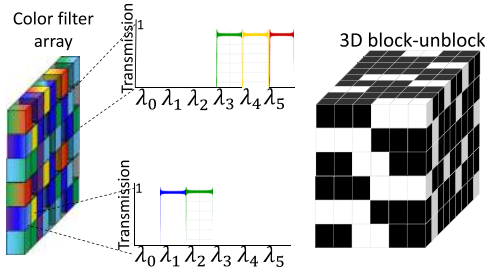

Fig. 1. Equivalence between 2D color coded aperture and 3D block-unblock coded aperture. The colored filters array is composed of spectral filters that modulate the transmittance of the incoming light in the system.

The fundamental characteristic of adaptive measurements is that they are more outstandingly robust to Gaussian noise than traditional non-adaptive measurements [21]. Furthermore, the intuition in adaptive sampling is always to use previous knowledge to adjust tunable parameters related with the CS acquisition system, such as the covariance matrix or a low-resolution reconstruction. The advantages of adaptive sampling include coding according to the scene, robustness to noise, and better quality of image reconstruction in comparison with conventional non-adaptive sampling systems. This work presents a gradient thresholding algorithm (GTA) to adaptively compute a color coded aperture to improve the quality of image reconstruction in C-CASSI. The intuition behind the adaptive sampling strategy is to design the CCA according to the most significant spectral signatures present in the scene. For that reason, a low-resolution spectral data cube is estimated, which is then interpolated to compute the second derivative of the spectral signatures. The second derivative of each spectral signature is then thresholded to detect the local maximum of each spectral signature. The transmittance of the CCA is established higher in the region of local maximum than in the local minimum in order to promote the spectral borders. The intuition here is that adaptively sensing the spectral borders improves the quality of image reconstruction.

This paper is divided into three sections: Section 2 gives a brief overview of the methods, specifically, the mathematical model of C-CASSI, the non-adaptive matrix representation of the sampling phenomenon, the proposed adaptive system, and the gradient thresholding algorithm (GTA). In Section 3,

simulation results show that the proposed adaptive C-CASSI outperforms the non-adaptive C-CASSI by up to 3 dB in terms of peak signal-to-noise ratio (PSNR). In Section 4, an implementation of the adaptive C-CASSI along with reconstruction of real experimental data is shown, comparing the adaptive versus the conventional non-adaptive methodologies.

2. METHODS

A. Color Coded Aperture Snapshot Spectral Imaging System

The continuous mathematical model of C-CASSI is given in Eq. (1). The color coded aperture $T(x,y,\lambda)$ modulates the incoming light $F(x,y,\lambda)$, where (x,y) represent the spatial coordinates and λ the wavelength. The coded density is then spread out by the dispersive element and captured in the sensor as

$$Y(x,y) = \iiint T(x',y',\lambda)F(x',y',\lambda)h(x'-S(\lambda)-x,y'-y)\mathrm{d}x'\mathrm{d}y'\mathrm{d}\lambda, \tag{1}$$

where $h(x'-S(\lambda)-x,y'-y)$ denotes the optical impulse response of the system, with $S(\lambda)$ being the dispersion generated by the prism. Each discrete voxel of the data cube, denoted as F_{ijk}, can be represented from the continuous source as

$$\begin{aligned} F_{ijk} &= \int_{\lambda_k}^{\lambda_{k+1}}\int_{j\Delta}^{(j+1)\Delta}\int_{i\Delta}^{(i+1)\Delta} F(x,y,\lambda)\mathrm{d}x\mathrm{d}y\mathrm{d}\lambda \\ &= c_{ijk}\cdot F(x_i,y_j,\gamma_k), \end{aligned} \tag{2}$$

for $i,j=0,\ldots,N-1$, $k=0,\ldots,L-1$ where c_{ijk} denotes the quadrature weight, and (x_i,y_j,γ_k) index the coordinates of the (i,j,k)th voxel, where i and j index the spatial coordinates and k the spectral axis. Let Δ be the pixel pitch of the detector and let λ_k the spectral discretization. The range of the kth spectral band is given by $[\lambda_k,\lambda_{k+1}]$ where λ_k is the solution to the equation $S(\lambda_{k+1})-S(\lambda_k)=\Delta$. Let $T^{\ell}_{i,j,k}\in\{0,1\}$ be the discretization of the color coded aperture $T^{\ell}(x,y,\lambda)$ used in the ℓ-th snapshot, $\ell=0,\ldots,K-1$, such that

$$T^{\ell}(x,y,\lambda) = \sum_{ijk} T^{\ell}_{ijk}\,\mathrm{rect}\left(\frac{x}{\Delta}-i-\frac{1}{2},\frac{y}{\Delta}-j-\frac{1}{2},\frac{\lambda}{\sigma_k}-k-\frac{1}{2}\right), \tag{3}$$

where Δ is the side length of the coded aperture, and $\sigma_k=\lambda_{k+1}-\lambda_k$. Notice that the index i is in the direction orthogonal to dispersion, and j is along the axis of dispersion. As shown in Eq. (3), the color coded aperture can be regarded as a 3D structure T^{ℓ}_{ijk}, whereas the traditional block-unblock coded aperture is a 2D structure. The ℓ^{th} discretized compressive measurement in C-CASSI can then be written as

$$Y^{\ell}_{i,l} = \sum_{k=0}^{L-1} F_{i,(l+k),k}\,T^{\ell}_{i,(l+k),k} + \omega_{i,l}, \tag{4}$$

where $Y^{\ell}_{i,l}$ is the intensity in the $(i,l)^{\text{th}}$ sensor pixel, where $l\in\{0,\cdots,N+L-1\}$, and $\omega_{i,l}$ is the Gaussian noise in the $(i,l)^{\text{th}}$ position, $i=0,\cdots,N-1$; notice that index l is along the axis of dispersion. The measurements in each snapshot can be arranged as $\mathbf{Y}^{\ell}\in\mathbb{R}^{N\times(N+L-1)}$. Similarly, the underlying scene can be denoted as $\mathbf{F}\in\mathbb{R}^{N\times N\times L}$, and $\mathbf{T}\in\mathbb{R}^{N\times N\times L}$ is a binary three-dimensional array modeling the color coded aperture. The compressive measurements in C-CASSI can then be expressed in matrix form as

$$\mathbf{y}^{\ell} = \mathbf{H}^{\ell}\mathbf{f} + \boldsymbol{\omega}, \tag{5}$$

where $\mathbf{H}^{\ell}$ stands for the ℓ^{th} sensing matrix, $\mathbf{f}$ denotes the vectorization of the underlying data cube $\mathbf{F}$, and $\boldsymbol{\omega}$ is the vectorization of the Gaussian noise. The vectorization of the matrix $\mathbf{F}$ is given by $(\mathbf{f}_k)^{\ell}_p=\mathbf{F}^{\ell}_{(p-rN)rk}$, for $p=0,\cdots,N^2-1$, $r=\lfloor p/N\rfloor$. Equation (5) can be rewritten as

$$\mathbf{y} = \overbrace{\begin{bmatrix} \mathrm{diag}(\mathbf{H}^{\ell}_0) & \mathrm{diag}(\mathbf{0}^0_{N(1)\times N^2}) & \cdots & \mathrm{diag}(\mathbf{0}^0_{N(L-1)\times N^2}) \\ & \mathrm{diag}(\mathbf{H}^{\ell}_1) & \cdots & \\ & & \ddots & \\ \mathrm{diag}(\mathbf{0}^0_{N(L-1)\times N^2}) & \mathrm{diag}(\mathbf{0}^0_{N(L-2)\times N^2}) & \cdots & \mathrm{diag}(\mathbf{H}^{\ell-1}_{L-1}) \end{bmatrix}}^{\mathbf{H}^{\ell}} \begin{bmatrix} \mathbf{f}_0 \\ \mathbf{f}_1 \\ \vdots \\ \mathbf{f}_{L-1} \end{bmatrix} + \boldsymbol{\omega}, \tag{6}$$

where $\mathrm{diag}(\mathbf{H}^{\ell}_k)$ is an $N^2\times N^2$ diagonal matrix whose entries are the elements of the ℓ^{th} vectorized color coded aperture of the k^{th} spectral band. Figure 2 depicts an example of the sensing matrix $\mathbf{H}=[(\mathbf{H}^0)^T,(\mathbf{H}^1)^T,\ldots(\mathbf{H}^{K-1})^T]^T$, for $K=2$, $N=6$, and $L=4$. Notice that $\mathbf{H}$ can be constructed as a sparse matrix since it is mostly populated with zeros; thus, its very large dimensions are easily manageable. t^{ℓ}_k is a vector that represents the non-zero elements in the k^{th} spectral band and the ℓ^{th} snapshot. The black squares represent blocking (zero-valued) elements, and the green, magenta, red, and yellow squares represent transmissive (one-valued) elements at the respective wavelengths.

B. Adaptive Color Coded Aperture

Figure 3 depicts the scheme of adaptive C-CASSI. In detail, the optical architecture inside the green dotted box corresponds to

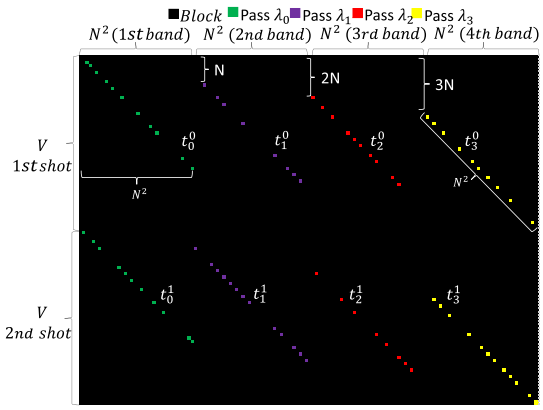

Fig. 2. Sensing matrix $\mathbf{H}$ where $K = 2$, $N = 6$, and $L = 4$, and $V = N(N + L - 1) = 54$. Black squares represent a zero-value element (blocking light). Green, magenta, red, and yellow squares represent one-value element (unblocking light) in the corresponding spectral band λ_0, λ_1, λ_2, and λ_3.

the C-CASSI system. The red dashed box denotes the proposed adaptive scheme that corresponds to the steps 3–7 of Algorithm 1. The gradient thresholding algorithm (GTA) algorithm was developed in order to design the CCA used in the next projection of the adaptive C-CASSI. The goal of the GTA algorithm is to enhance the spectral borders of the reconstructed data cube, with the intuition that adaptively sensing the spectral borders improves the quality of image reconstruction. In particular, the steps of the proposed adaptive system are: low-resolution reconstruction, interpolation of the low-resolution data cube, computation of the spectral gradient, thresholding of the spectral gradient, and adjustment of the transmittance of the spectral filter. The inputs of the GTA algorithm are the initial compressive measurements $\mathbf{y}^0$ and the initial sensing matrix $\mathbf{H}^0$.

The first step denoted as (I) in Fig. 3 is the computation of a low-resolution data cube from $\mathbf{y}^0$ and $\mathbf{H}^0$. This low-resolution estimation is done, since it is difficult to extract information about the scene from the compressed measurement directly, and a full-resolution data cube reconstruction demands higher computational complexity. Some other works extract borders by employing side information from a second sensor placed aside the sensing device [22]. Although this reconstruction is not in real time, this penalty is tolerable for the adaptive design of CCA. GTA exploits the low-resolution data cube, which provides prior information about the underlying scene $\mathbf{f}$. Formally, let $\mathbf{f}_L^\ell = \mathbf{D}\mathbf{f}$, be the vectorized low-resolution image where $\mathbf{D}$ denotes the decimation matrix and $\mathbf{f}$ identifies the underlying scene. The low-resolution version $\hat{\mathbf{f}}_L^\ell$ is obtained by solving

$$\hat{\mathbf{f}}_L^\ell = \Psi_L\Big(\arg\min_{\boldsymbol{\theta}_L}\|\mathbf{y} - \mathbf{H}_L^\ell\boldsymbol{\Psi}_L\boldsymbol{\theta}_L\|_2^2 + \tau\|\boldsymbol{\theta}_L\|_1 + \lambda\|(\mathbf{C} - \mathbf{I})(\boldsymbol{\Psi}_L\boldsymbol{\theta}_L)\|_2^2\Big), \tag{7}$$

where $\mathbf{H}_L^\ell = \mathbf{H}^\ell\mathbf{D}$ denotes the decimated sensing matrix, $\boldsymbol{\Psi}_L$ is the representation basis, and $\boldsymbol{\theta}_L$ is the vectorization of a sparse vector for the low-resolution reconstruction, $\mathbf{I}$ is the identity matrix, $\mathbf{C}$ is a Gaussian filter to promote smoothness, and τ, λ are regularization constants.

This low-resolution data cube $\hat{F}_L^0$ is then interpolated to obtain a high-resolution data cube $\hat{F}_H^0$, as shown in Fig. 3(II). In particular, step 4 of the GTA algorithm performs the interpolation of the low-resolution data cube by using $\hat{\mathbf{f}}_H^\ell \leftarrow \mathbf{P}\hat{\mathbf{f}}_L^\ell$ where the interpolator $\mathbf{P}$ is a bilinear interpolator attaining a high-resolution data cube $\hat{\mathbf{f}}_H^\ell$. In the following step, the spectral gradient $\mathbf{S}^\ell$ is computed, as depicted in Fig. 3(III). More precisely, $\mathbf{S}^\ell$ is the discrete second derivative of each spectral signature, also referred to as the spectral borders. The spectral gradient computation of the high-resolution data cube is performed as $\mathbf{s}^\ell \leftarrow \mathbf{B}^2\hat{\mathbf{f}}_H^\ell$ (line 5, GTA), where ℓ refers to the ℓ^{th} snapshot, $\mathbf{B}^2$ computes the second derivative of the spectral signature, with $\mathbf{B} \in \mathbb{R}^{N^2L\times N^2L}$ being the gradient matrix given by

$$\mathbf{B} = \mathbf{G} \otimes \mathbf{I}, \tag{8}$$

where $\mathbf{I} \in \mathbb{R}^{N^2\times N^2}$ is an identity matrix, $\otimes$ is the Kronecker product, and $\mathbf{G} \in \mathbb{R}^{L\times L}$ is denoted as

$$\mathbf{G} = \begin{pmatrix} -1 & 1 & 0 & 0 & \cdots & 0 & 0 & 0 & 0 \\ -0.5 & 0 & 0.5 & 0 & \cdots & 0 & 0 & 0 & 0 \\ 0 & -0.5 & 0 & 0.5 & \cdots & 0 & 0 & 0 & 0 \\ \vdots & \vdots & \vdots & \vdots & \ddots & \vdots & \vdots & \vdots & \vdots \\ 0 & 0 & 0 & 0 & \ddots & -0.5 & 0 & 0.5 & 0 \\ 0 & 0 & 0 & 0 & \cdots & 0 & -0.5 & 0 & 0.5 \\ 0 & 0 & 0 & 0 & \cdots & 0 & 0 & -1 & 1 \end{pmatrix}. \tag{9}$$

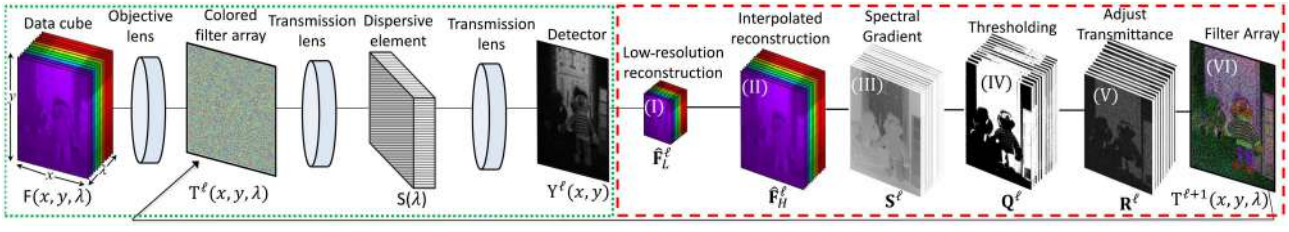

Fig. 3. System layout of the adaptive C-CASSI. The scheme depicts two snapshots of C-CASSI. In the first snapshot, the color coded aperture $\mathbf{T}^\ell$ is generated randomly. In the second snapshot, the color coded aperture $T^{\ell+1}(x, y, \lambda)$ is adaptively designed by the GTA, (I) using as prior information a low-resolution reconstruction $\mathbf{F}_L^\ell$, (II) the reconstruction is interpolated $\mathbf{F}_H^\ell$, (III) then the spectral edges of the interpolated data cube are computed $\mathbf{S}^\ell$, (IV) the gradient is thresholded $\mathbf{Q}^\ell$, and (V) the transmittance is adjusted $T^{\ell+1}(x, y, \lambda)$. This process repeats for the subsequent snapshots.

The matrix $\mathbf{G}$ computes the central differences in the internal data points and the single-side differences along the edges. Each row of the matrix $\mathbf{G}$ computes the pixel-wise central difference of the spectral signature [23]. The matrix $\mathbf{B}$ computes the central differences for all the spectral signatures in the data cube. Similarly, notice that $\mathbf{B}^2$ finds the second derivative of each spectral signature of the high-resolution data cube by calculating $\mathbf{B}^2\hat{\mathbf{f}}_H^{\ell}$. Therefore, the gradient $\mathbf{s}^{\ell}$ is referred to as the spectral borders. The next step is to compute the thresholding of the gradient to identify the maximum $\mathbf{Q}^{\ell}$ and minimum local spectral intensity regions $1 - \mathbf{Q}^{\ell}$, where $\mathbf{Q}^{\ell}$ is a binary cube with ones in the maximum spectrum, and $1 - \mathbf{Q}^{\ell}$ is a binary cube with ones in the minimum spectrum, i.e. the negative of $\mathbf{Q}^{\ell}$. The thresholding of the gradient is performed according to the logical operation $\mathbf{q}^{\ell} \leftarrow (\mathbf{s}^{\ell} \preceq \mathbf{0})$ (line 6, GTA), where $\mathbf{q}^{\ell}$ is the vectorization of $\mathbf{Q}$, $\preceq$ is the element-wise inequality, $\mathbf{s}^{\ell}$ is the computed gradient, and $\mathbf{0}$ is an all-zero vector. The thresholding $\mathbf{s}^{\ell} \preceq \mathbf{0}$ splits the spectral intensity profile in a maximum local spectral intensity region $\mathbf{q}^{\ell}$ and a minimum local spectral intensity region $\mathbf{1} - \mathbf{q}^{\ell}$, which corresponds to the complement of $\mathbf{q}^{\ell}$. This approach enhances the spectral borders across each spectral profile by sampling with different transmittances the high and low spectral intensities. The transmittance is the percentage of light that hits the FPA. The transmittance is set according to the maximum and minimum spectral intensities.

Algorithm 1: GTA gradient thresholding algorithm.

Require: $\mathbf{y} \leftarrow [\mathbf{y}^0]^T$, $\mathbf{H} \leftarrow [\mathbf{H}^0]^T$
Ensure: $\hat{\mathbf{f}}$
1: **function** GTA ($\mathbf{y}$, $\mathbf{H}$, $\mathbf{B}$)
2: **for** $\ell \leftarrow 0, K-1$ **do**
3: $\hat{\mathbf{f}}_L^{\ell} \leftarrow \mathbf{\Psi}_L \Big(\arg\min_{\boldsymbol{\theta}_L} \|\mathbf{y} - \mathbf{H}_L \mathbf{\Psi}_L \boldsymbol{\theta}_L\|_2^2 + \tau\|\boldsymbol{\theta}_L\|_1 + \lambda\|(\mathbf{C} - \mathbf{I})(\mathbf{\Psi}_L \boldsymbol{\theta}_L)\|_2^2 \Big)$ ▷ Low-resolution
4: $\hat{\mathbf{f}}_H^{\ell} \leftarrow \mathbf{P}\hat{\mathbf{f}}_L^{\ell}$ ▷ Interpolation
5: $\mathbf{s}^{\ell} \leftarrow \mathbf{B}^2\hat{\mathbf{f}}_H^{\ell}$ ▷ Compute gradient
6: $\mathbf{q}^{\ell} \leftarrow (\mathbf{s}^{\ell} \preceq \mathbf{0})$ ▷ Thresholding
7: $\mathbf{r}^{\ell} \leftarrow \mathbf{q}^{\ell} \odot \mathbf{r}_d^{\ell} + (\mathbf{1} - \mathbf{q}^{\ell}) \odot \mathbf{r}_u^{\ell}$, ▷ Transmittance
8: **for** $n \leftarrow 0, N^2L - 1$ **do**
9: $k = \lfloor n/N^2 \rfloor$, $l = n \bmod N^2$
10: $(r_k^{\ell})_l \leftarrow r_n^{\ell}$ ▷ Rearrange $\mathbf{r}$
11: **for** $m \leftarrow 0, KV - 1$ **do**
12: **if** $m - \ell_m V = n - k_n(N^2 - N)$ **then**
13: $(H_m^{\ell+1})_n \leftarrow (r_{k_n}^{\ell_m})_{m-\ell_m v - k_n N}$ ▷ Compute $\mathbf{H}$
14: **else**
15: $(H_m^{\ell+1})_n \leftarrow 0$
16: $\mathbf{y}^{\ell+1} \leftarrow \mathbf{H}^{\ell+1}\mathbf{f}$ ▷ Next snapshot
17: $\mathbf{y} \leftarrow [(\mathbf{y}^0)^T, \ldots (\mathbf{y}^{K-1})^T]^T$
18: $\mathbf{H} \leftarrow [(\mathbf{H}^0)^T, \ldots (\mathbf{H}^{K-1})^T]^T$
19: **return** $\hat{\mathbf{f}} \leftarrow \mathbf{\Psi}(\arg\min_{\boldsymbol{\theta}} \|\mathbf{y} - \mathbf{H}\mathbf{\Psi}\boldsymbol{\theta}\|_2^2 + \tau\|\boldsymbol{\theta}\|_1)$

The adjustment of transmittance denoted as $\mathbf{R}^{\ell}$ shown in Fig. 3(V) sets a higher transmittance η_d in the local maximum intensity region $\mathbf{Q}^{\ell}$, and a lower transmittance η_u in the local minimum intensity region $\mathbf{1} - \mathbf{Q}^{\ell}$, where $\eta_d \geq \eta_u$. In step 7 of GTA, a vectorization version of the adaptive color coded aperture is computed according to $\mathbf{r}^{\ell} \leftarrow \mathbf{q}^{\ell} \odot \mathbf{r}_d^{\ell} + (\mathbf{1} - \mathbf{q}^{\ell}) \odot \mathbf{r}_u^{\ell}$, where $\mathbf{r}_d^{\ell}$ and $\mathbf{r}_u^{\ell}$ are vectors with binary entries and transmittance functions $\eta_d[\ell]$ and $\eta_u[\ell]$, respectively, dependent on the number of snapshots as the following:

$$\mathbf{r}_d^{\ell} \sim \begin{cases} \text{Ber}(\eta_d[\ell] = 0.5), & \text{if } \ell = 0 \\ \text{Ber}(\eta_d[\ell] = 2/(\ell + 3)), & \text{otherwise,} \end{cases} \tag{10}$$

$$\mathbf{r}_u^{\ell} \sim \begin{cases} \text{Ber}(\eta_u[\ell] = 0.5), & \text{if } \ell = 0 \\ \text{Ber}(\eta_u[\ell] = 1/(\ell + 1)), & \text{otherwise.} \end{cases} \tag{11}$$

This step represents the adjustment of the transmittance. The adjustment in transmittance emphasizes the spectral borders $\mathbb{S}^{\ell}$, where Ber$(\cdot)$ denotes the Bernoulli distribution. The intuition behind these transmittance functions builds on a state-of-the-art transmittance criterion for color coded apertures [24]. In particular, $\mathbf{r}_u^{\ell}$ is a transmittance criterion for color coded apertures for $\ell > 0$, defined as the inverse of the number of snapshots. This criterion reduces the transmittance of the color coded aperture as the number of snapshots increases. In order to promote the spectral borders, two different transmittances are used in this paper, such that $\mathbf{r}_u^{\ell} \leq \mathbf{r}_d^{\ell}$. The values of these transmittance functions are close to those theoretically found in Ref. [24] but were found through experimentation in this paper. In particular, we set the transmittance $\mathbf{r}_d^{\ell}$ to be higher than $\mathbf{r}_u^{\ell}$ because we want to sample the local maximum spectral intensity region $\mathbf{q}^{\ell}$ more. This in turn permits us to sample the higher intensities more to sharpen the profiles of the spectral bands [25]. $\mathbf{R}^{\ell}$ then enhances the spectral borders of the reconstructed data cube by increasing the transmittance in the abrupt spectral intensity changes of the interpolated data cube. The transmittance parameters of $\mathbf{r}_d^{\ell}$, $\mathbf{r}_u^{\ell}$ were found after exhaustive search in the range between 0.1 and 0.9.

According to Eq. (10), for the first snapshot, the sampling vector $\mathbf{r}_d \sim \text{Ber}(\eta_d[\ell] = 0.5)$ has a transmittance function $\eta_d[\ell] = 0.5$ for the local maximum spectral intensity region $\mathbf{q}^{\ell}$. When the number of snapshots is $\ell > 0$, the sampling vector is given by $\mathbf{r}_d \sim \text{Ber}(\eta_d[\ell] = 2/(\ell + 3))$ with transmittance function denoted by $\eta_d[\ell] = 2/(\ell + 3)$. Also, as stated in Eq. (11), for the first snapshot, the sampling vector $\mathbf{r}_u \sim \text{Ber}(\eta_u[\ell] = 0.5)$ has a transmittance $\eta_u[\ell] = 0.5$ for the local minimum spectra intensity $\mathbf{1} - \mathbf{q}^{\ell}$. When the number of snapshots is $\ell > 0$, the sampling vector is $\mathbf{r}_u \sim \text{Ber}(\eta_u[\ell] = 1/(\ell + 1))$, the transmittance function of which is $\eta_u[\ell] = 1/(\ell + 1)$. The intuition behind the transmittance adjustment comes from Gonzalez and Woods, who classified the edge models according to intensity profiles [25]. In general, it is known that digital images are contaminated with blurring due to the focusing mechanism and noise because of the electronic components. The two most accurate edge models are the intensity ramp profile and the roof edge profile [25]. The transmittance adjustment of GTA is designed based on these edge models. The output of the algorithm is the subsequent filter array $T(x, y, \lambda)^{\ell+1}$ shown in Fig. 3(VI). Particularly, the proposed design increases the transmittance in some areas of $\mathbf{H}$ and decreases it in others. Let H_{mn} denote each entry of $\mathbf{H}$, if $\text{H}_{mn} = 1$ the light gets into the system and if $\text{H}_{mn} = 0$ the light is filtered out from reaching the FPA, where $m = 0, \ldots, K(N + L - 1) - 1$; $n = 0, \ldots, N^2L - 1$.

The last steps of the algorithm rearrange the vectorization version of $\mathbf{r}^{\ell}$ to its matrix version $\mathbf{H}^{\ell+1}$. In more detail,

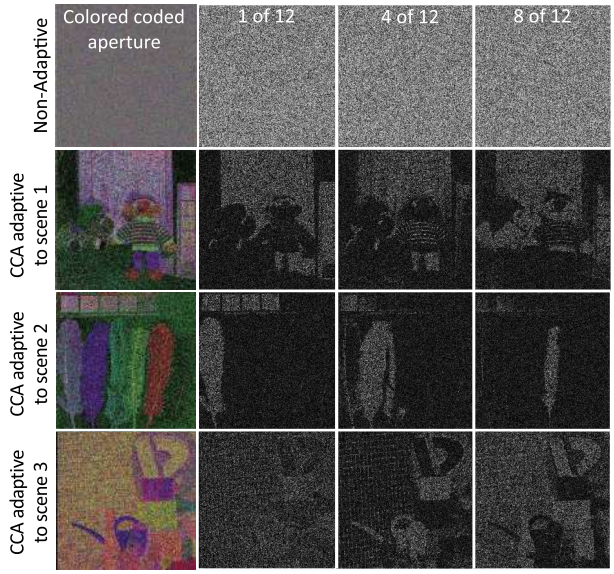

Fig. 4. Comparison between non-adaptive and adaptive color coded apertures when $K = 6$. The top row depicts non-adaptive random patterns. The second, third, and fourth rows show adaptively designed apertures, resulting from the use of the proposed algorithm, highly correlated with the spectral bands of each scene. (First column) CCA; (second column) three slices of the 3D block-unblock representation.

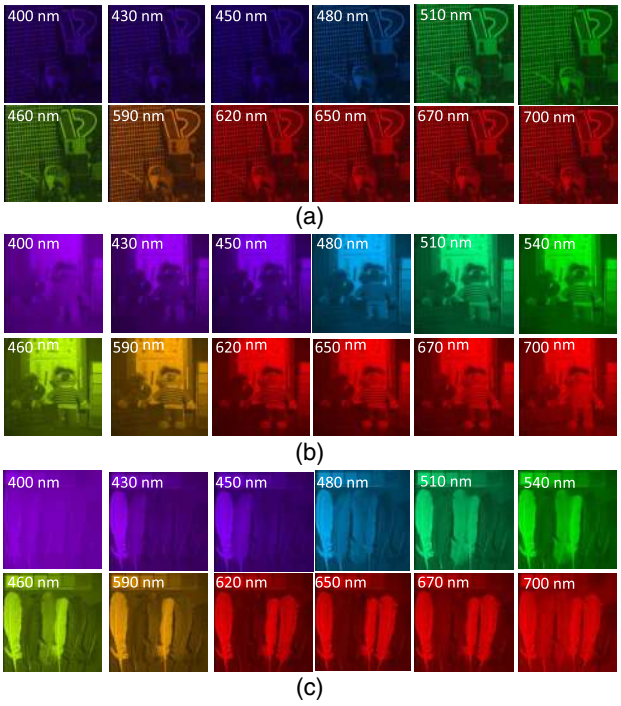

Fig. 5. Three spectral scenes are used to test the proposed adaptive approach. These scenes have a resolution of 512 × 512 × 12 pixels, and they span a spectral range between 400 and 700 nm. Figures (a)–(c) depict 12 spectral bands with the corresponding central wavelength of the database of scene 5 from Ref. [27], chart and stuffed toys, and feathers from Ref. [28].

in step 10, the vector $\mathbf{r}^{\ell}$ is rearranged as the 2D k^{th} plane according to $(\mathbf{r}_k^{\ell})_l \leftarrow \mathbf{r}_n^{\ell}$. Afterwards, in step 13, the vectorization of the color coded aperture $\mathbf{r}^{\ell}$ is stacked in the sensing matrix $\mathbf{H}^{\ell}$ according to $(H_m^{\ell+1})_n \leftarrow (r_{k_n}^{\ell_m})_{m-\ell_m v-k_n N}$, $k_n = \lfloor n/N^2 \rfloor$, $\ell_m = \lfloor m/V \rfloor$, $\ell_m \in \{0, \ldots, K-1\}$. In step 16, the adaptive snapshot is captured as $\mathbf{y}^{\ell+1} \leftarrow \mathbf{H}^{\ell+1}\mathbf{f}$. In step 19, the output of algorithm 1 is the approximation $\hat{\mathbf{f}}$. At each snapshot, the GTA algorithm is computed because the quality of the low-resolution data cube increases with each additional snapshot. Examples of the coding patterns designed by the proposed algorithm are depicted in Fig. 4. These coding patterns show the color coded aperture along a set of axial slices of the 3D block-unblock representation. Specifically, Fig. 4 depicts a comparison between non-adaptive CCA and adaptive CCA. In detail, the first row depicts the non-adaptive color coded aperture. The second, third, and fourth rows show the adaptive coded apertures for three different spectral scenes. The first row depicts non-adaptive CCA. The second through fourth rows of Fig. 4 show the adaptive CCA. The first column depicts the CCAs. The second through fourth columns show 3 out of 12 axial slices of the block-unblock representation. The total number of axial slices is the same as the number of spectral bands, in this case $L = 12$. Notice that each color coded aperture is highly correlated with the corresponding scene. The scenes are illustrated in Fig. 5. The adaptive filter arrays resemble the spectral components of the corresponding scene.

3. SIMULATIONS

To assess the capabilities of the adaptive C-CASSI, it is compared with the non-adaptive C-CASSI. A critical parameter in the simulations is the transmittance, which is traditionally set to 50% in non-adaptive C-CASSI. In adaptive C-CASSI, the transmittance is set according to two important regions, local maximum $\mathbf{q}^{\ell}$ and local minimum $\mathbf{1} - \mathbf{q}^{\ell}$ spectral intensity regions. This process emphasizes the spectral borders $\mathbf{s}^{\ell}$, according to the intensity profile edge model [25]. The GTA algorithm 1 uses transmittance functions that reduce the transmittance of the color coded apertures as the number of snapshots increases, $\eta_d[\ell]$, $\eta_u[\ell]$, where $\eta_d[\ell] \geq \eta_u[\ell]$. Equations (10) and (11) determine the transmittance in the adaptive approach. GTA algorithm 1 uses the Gradient Projection for Sparse Reconstruction (GPSR) algorithm [26] to solve step 3 and step 19. The type of GPSR used in this paper is the Barzilai–Borwein gradient projection (GPSR-BB). For the reconstruction, the basis representation $\mathbf{\Psi}$ is set to be the Kronecker product of three bases, $\mathbf{\Psi} = \mathbf{\Psi}_1 \otimes \mathbf{\Psi}_2 \otimes \mathbf{\Psi}_3$. The 2D spatial representation basis $\mathbf{\Psi}_{2D} = \mathbf{\Psi}_1 \otimes \mathbf{\Psi}_2$ is the 2D-wavelet symmlet 8 basis, and the spectral sparsifier is the 1D cosine transform basis $\mathbf{\Psi}_3$. The input measurements $(\mathbf{y})$ in the GTA algorithm were acquired using Eq. (5), including a Gaussian noise with SNR = 10 dB. The GTA algorithm was evaluated with three scenes shown in Fig. 5. The first database is a portion of scene 5 from [27], [Fig. 5(a)]; the second database is the chart and stuffed toys from [28], [Fig. 5(b)]; and the third database is the feathers also from [28], [Fig. 5(c)]. Each spectral data cube has 12 bands that span between 400 and 700 nm, and the spatial resolution is 512 × 512 pixels.

Figures 5(a)–5(c) depict 12 spectral bands of scene 5 in Ref. [27], chart and stuffed toys, and feathers in Ref. [28]. Each spectral band has its corresponding central wavelengths.

Figure 6 illustrates a comparison of the averaged PSNR against the number of snapshots for each database. Each subplot compares the quality of image reconstruction for the non-adaptive C-CASSI and the adaptive C-CASSI. Each column of the figure depicts experiments using scene 5, chart and stuffed toy, and the feathers database, respectively. Each row refers to a certain signal-to-noise ratio (SNR) scenario for each database; the corresponding SNR for each row is 10, 20, 50, and 100 dB, respectively. Note that when the number of snapshots is less than or equal to two, the transmittance is 50% for both approaches; therefore, at that snapshot level, there is not a significant difference. In contrast, after the second snapshot, the adaptive method overcomes the traditional approach. The simulations reveal that in the presence of noise, the traditional approach is outperformed by the proposed adaptive approach in up to 2 dB. The results highlight the importance of adapting the subsequent colored apertures according to the previous information gathered in the compressive measurements. A remarkable result from the simulations is that the non-adaptive C-CASSI is less robust to Gaussian noise than the proposed adaptive C-CASSI. In order to show the scalability of the adaptive C-CASSI, Fig. 7 shows the results of the quality of image reconstruction against the number of snapshots when the databases exhibit $L = 24$ spectral bands. The simulations show that the adaptive C-CASSI overcomes the non-adaptive up to 3 dB. In order to compare the traditional method and the proposed adaptive method, the PSNR is used to measure the quality of image reconstruction. Figure 8 shows a zoomed version of the toy and the stuff scene. In the first row, it is depicted as the original scene. The second row shows the result of the non-adaptive C-CASSI, and the third row shows the result of the proposed adaptive method. Four out of the 12 wavebands are shown with their corresponding central wavelength of 430, 480, 560, and 650 nm along with the attained PSNR. The PSNR of the reconstructed bands with the non-adaptive approach is lower in comparison with the adaptive C-CASSI. In fact, the averaged PSNR across the 12 spectral bands is 33.5 dB for the non-adaptive C-CASSI and 35.6 dB for the adaptive C-CASSI. To test the fidelity of the spectral reconstructions, three reference spectral signatures denoted as $P1$, $P2$, and $P3$ are compared against the reconstructed spectral signatures of non-adaptive and adaptive C-CASSI in Fig. 9. The root mean square error between the reference and the reconstruction are included in each subfigure to improve the understanding of the results. These results revealed that more similarity exists between the reference and the reconstructed spectral signatures using adaptive C-CASSI.

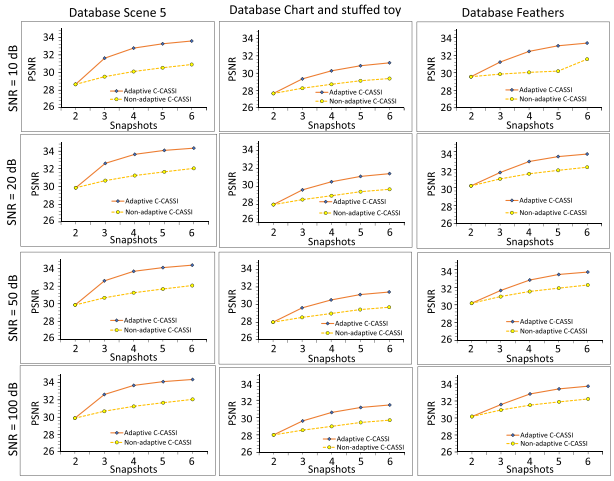

Fig. 6. Averaged PSNR against the number of snapshots for each spectral scene (columns of the image), under four different SNR scenarios 10, 20, 50, and 100 dB in the compressive measurements (rows of the image).

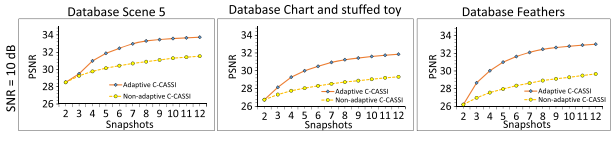

Fig. 7. Averaged PSNR against the number of snapshots for each spectral scene with $L = 24$ spectral bands and capturing $K = 12$ snapshots. The simulations include Gaussian noise with SNR = 10 dB in the compressive measurements.

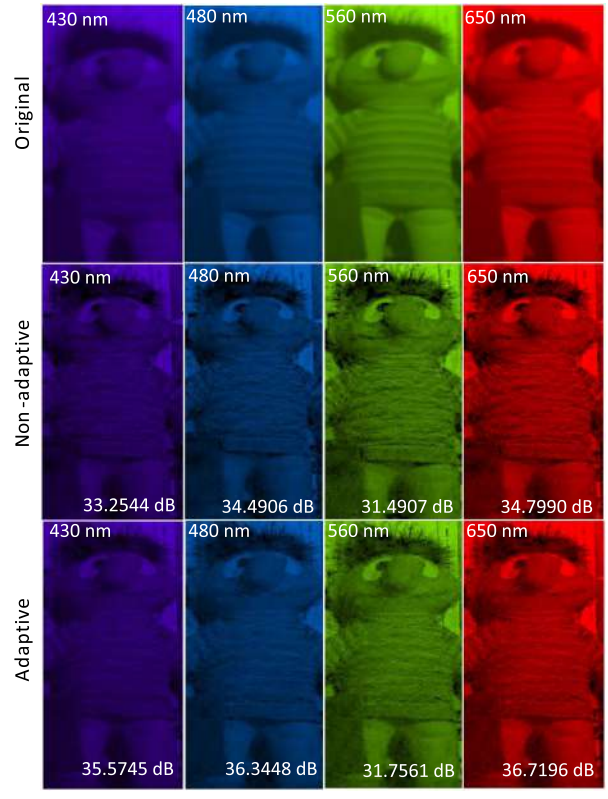

Fig. 8. Zoomed reconstruction of a subset of spectral bands using $K = 6$ snapshots for non-adaptive C-CASSI with average PSNR across the spectral bands 33.5 dB and compression ratio of 50%, and adaptive C-CASSI with average PSNR 35.6 dB and compression ratio of 80%. In addition, the PSNR for the specific band is indicated.

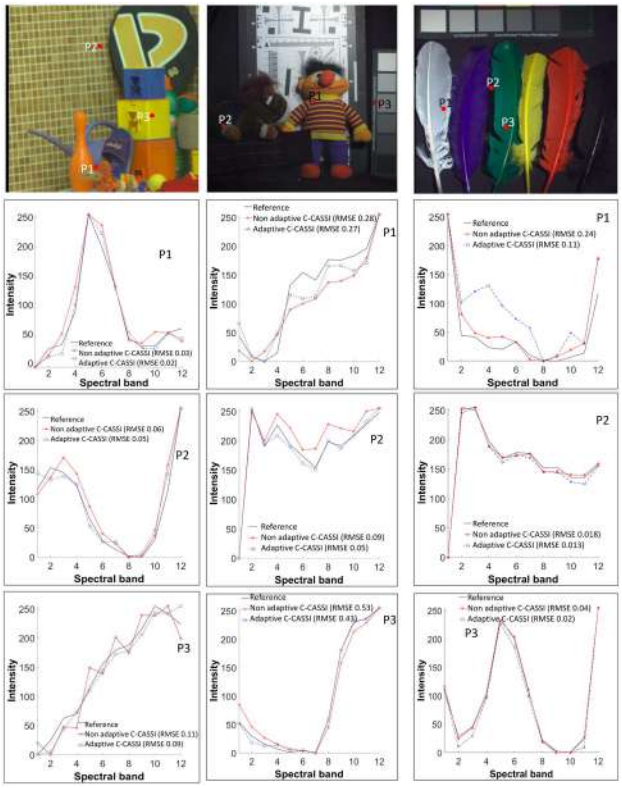

Fig. 9. Spectral fidelity analysis at three points ($P1$, $P2$, $P3$) for each scene. The reference spectral signature and the reconstructed spectral signatures of the non-adaptive and adaptive C-CASSI are compared. Note that the spectral signatures of the proposed adaptive C-CASSI approach are closer to the reference spectral signature than the traditional non-adaptive C-CASSI.

4. EXPERIMENTAL SETUP

To experimentally prove the advantage of the adaptive design against the traditional system, the C-CASSI was assembled in our laboratory as depicted in Fig. 10, in accordance with [15] using a DMD-based implementation of color coded apertures. The optical scheme depicts two arms: the imaging arm and the integration arm. In the imaging arm, the imaging lens focuses the light into the DMD. Due to the DMD rotation angle of 45° relative to the detector pixels, the alignment of the optical elements is critical. In order to correct for the inclination of the DMD, the elements in the integration arm of the setup are rotated 45°, including the relay lens, the filter wheel, the prism, and the FPA. The apparatus is made up of (1) an AC254-100-A-ML objective lens (Thorlabs), (2) a DLI4130 DMD (DLInnovations) with spatial resolution of 1024×768 and mirror pitch size of 13.68 μm, (3) a MAP10100100-A relay lens (Thorlabs), (4) an Amici Prism (Shanghai Optics), and (5) a monochrome charged-coupled device detector (AVT Stingray F-145B) with spatial resolution 1388×1038 and pitch size of 6.45 μm. The emulation of the CCA using the DMD and the set of optical filters is as follows: each CCA is mapped to a 3D array of block-unblock coded apertures paired with the corresponding set of optical filters, as described in Ref. [15], thus emulating T^{ℓ}_{ijk} in Eq. (3). Each pair of filter and block-unblock coded aperture is calibrated to characterize the impulse response of the system, which uses as input a monochromatic light and a white plate as the target. The compressive measurements are obtained using as a target the real scene instead of the white plate and replacing the monochromatic light with a broadband white light. If each band is set to be encoded independently, a single shot acquisition with L bands will require L switches in the DMD and L rotations of the filter wheel. Experimentally, the DMD switching time is ∼50 μs, and the rotation time of the filter wheel is ∼50 ms, being the latter the bottleneck. Therefore, the largest integration time for a single shot is bounded by 50 L ms. Two target scenes were used to evaluate the quality of image reconstruction of the adaptive C-CASSI against non-adaptive C-CASSI. Figure 11 depicts the two targets. In this setup, the 3D block-unblock representation of CCA is loaded in the DMD, and each 2D slice is paired with the corresponding color filter placed in the filter wheel. Afterwards, the measurements is obtained by adding the 2D measurements. The experimental setup is synchronized such that the DMD sets the pattern and the sensor captures the projection. After that, the DMD updates the coded aperture, and the filter wheel rotates. Subsequently, the detector measures the next projection. The first target is the bear-stars scene (left), and the second target is the flower-stars scene (right). The spatial resolution of the target scenes is 128×128. In the characterization of the Amici prism, $L = 11$ spectral bands are resolved. The corresponding wavelength intervals are: {423–436}; {437–448}; {449–463}; {464–479}; {480–499}; {500–521}; {522–546}; {547–577}; {578–618}; {619–673}; {674–700} nm. Due to the nonlinear

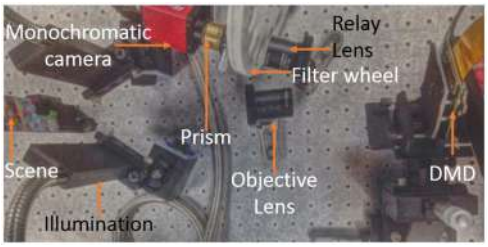

Fig. 10. Optical scheme of the DMD filter-wheel-based C-CASSI. In the imaging arm, the imaging lens focuses the scene in the DMD. In the integration arm, the relay lens focuses the encoded light by the DMD into the sensor after it is filtered by the filter wheel and dispersed by the prism. The synchronization control coordinates the change of filters of the filter wheel, the DMD switching, and integration of the sensor.

Fig. 11. Bear-stars scene (left). Flower-stars scene (right).

dispersion of the prism, the spectral bandwidths are different. In order to compare the reconstructed spectral signatures using the prism with the spectral signatures obtained with the commercial spectrometer, we select the values in the spectrometer readout corresponding to the central wavelength of the mentioned intervals. Figure 12 shows an RGB representation of the reconstructed data cubes of the bear-stars scene using $K = 4$ snapshots (first row) and the flower-stars scene (second row). The non-adaptive C-CASSI using random color coded aperture is shown in Figs. 12(a) and 12(c), and the proposed adaptive C-CASSI in Figs. 12(b) and 12(d). As can be observed, the proposed procedure improves the quality of image reconstruction. Four zoomed details of the scene are depicted in the insets of each subfigure, in Figs. 12(a) and 12(b), inset (I) the right of the bow tie, (II) the bear's nose, (III) the center bow tie, and (IV) the yellow star. Regarding the second scene, Fig. 12(c), 12(d) includes (I) the white space between two flowers, (II) the center of a flower in the bottom-right corner, (III) the pink star, and (IV) the light-blue background. In these zoomed details of the scene the improvement in the quality of image reconstruction of the proposed method is evident. Notice that the diagonal lines crossing the stars are more appreciable in the reconstruction with adaptive C-CASSI than in traditional C-CASSI due to the higher transmittance in the local maximum region in comparison with the local minimum region. Figure 13 represents a comparison of the reconstructed spectral bands of the bear scene using non-adaptive C-CASSI and adaptive C-CASSI with $K = 4$ snapshots for the spectral bands $\lambda_6 = 534$, $\lambda_7 = 562$, and $\lambda_8 = 597$ nm. In more detail, the first row depicts the spectral reconstruction using non-adaptive C-CASSI, and the second row shows the spectral reconstruction using adaptive C-CASSI. The same four zoomed details of the scene are depicted for each spectral band. In particular, notice for the proposed approach the better spectral quality in diagonal lines of zoomed details (I) and (IV). To test the fidelity of the spectral reconstruction, Fig. 14 shows the spectral signatures for three spatial positions **P1**, **P2**, **P3** of the bear-stars scene for $K = 3$ snapshots, and the flower-star scene for $K = 3$ snapshots. For the scene in the top row, the point **P1** corresponds to light-blue background, the **P2** represents the red bow tie, and **P3** denotes the yellow star. For the scene in the bottom row, the spatial points correspond to **P1**, the light-blue background; **P2**, the dark-red petal of the flower in the top-left corner; and **P3**, the orange petal of the flower in the bottom-right corner. In each spatial point the light is measured using an Ocean Optics Flame spectrometer. The resulting spectral signature is compared with the spectral signature for the reconstructions using the non-adaptive C-CASSI and the adaptive C-CASSI. The three subplots show the improvement in the quality of image reconstruction of the proposed adaptive method in the bear-stars scene and flower-stars scene in comparison with the traditional random method.

5. DISCUSSION

In this section, the proposed adaptive C-CASSI design is compared against the non-adaptive C-CASSI in terms of four aspects. The first aspect is reconstruction accuracy, in which the simulation and experimental results show that the reconstruction accuracy of adaptive C-CASSI is better than

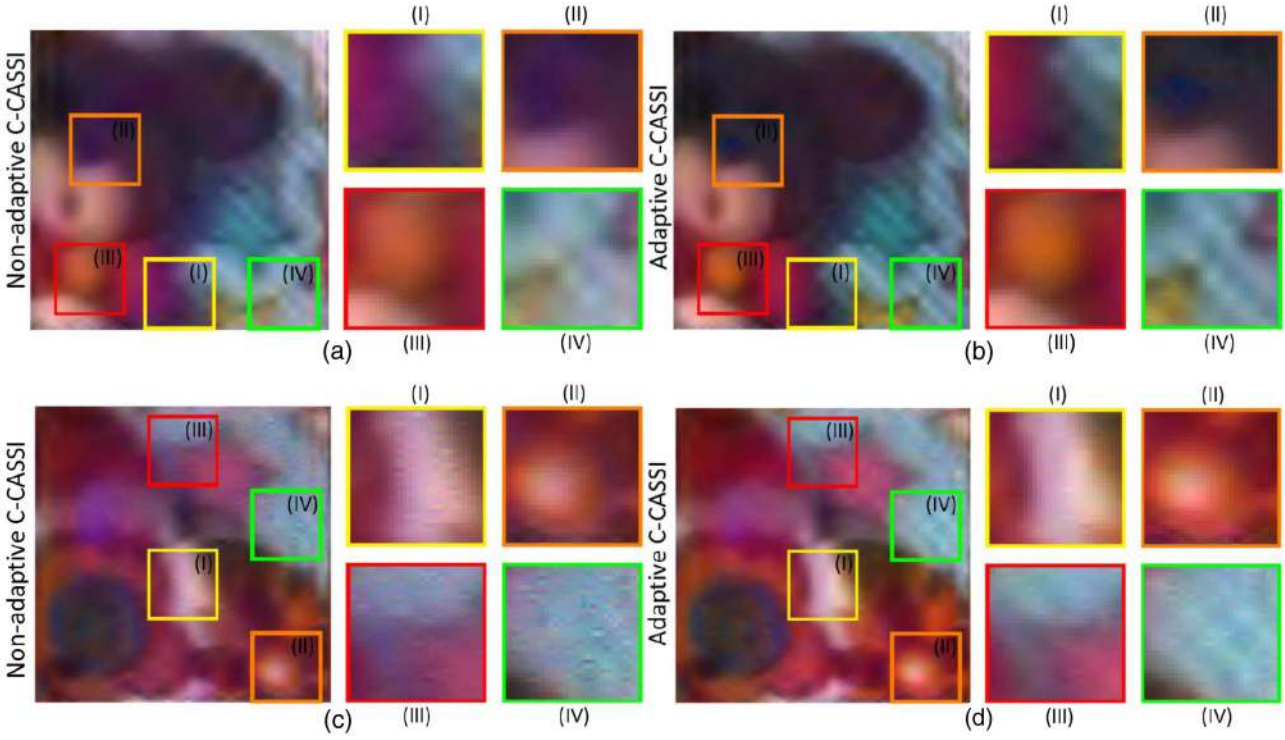

Fig. 12. RGB reconstruction of the bear-stars scene (first row), and the flowers-start scene (second row), using $K = 4$ snapshots with [(a) and (c)] the traditional C-CASSI and [(b) and (d)] the adaptive C-CASSI. Four zoomed sections (I)–(IV) are shown for each subfigure in order to easily appreciate the improvements.

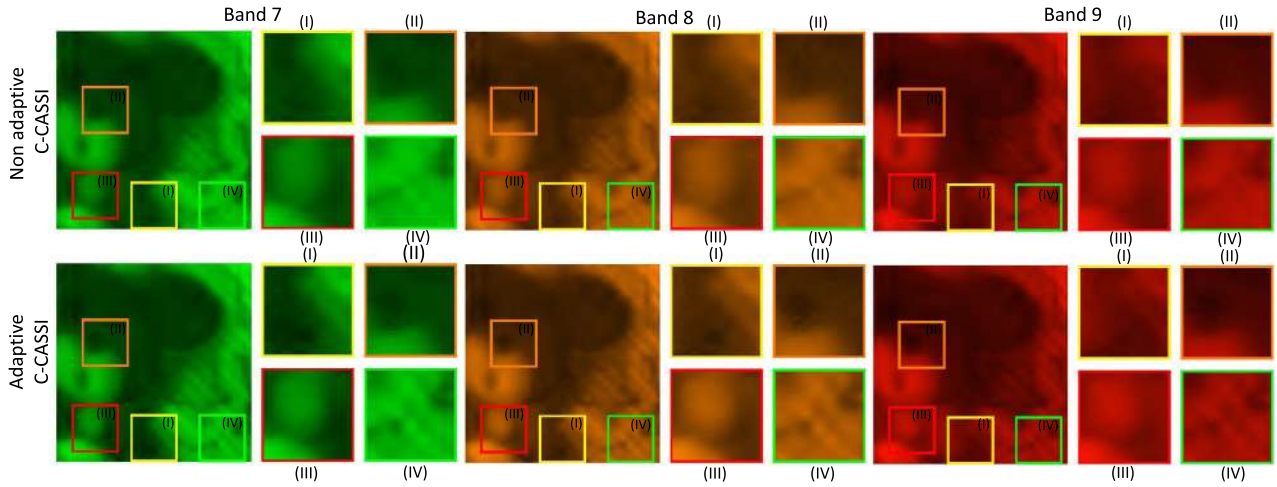

Fig. 13. Reconstruction bear-stars spectral scene at wavelengths $\lambda_6 = 534$ nm, $\lambda_7 = 562$ nm, and $\lambda_8 = 597$ nm. In the right of each spectral band there are shown four zoomed sections (I)–(IV). The first row depicts the recovered spectral band with traditional C-CASSI using $K = 4$ snapshots, whereas the second row shows the spectral reconstruction with adaptive C-CASSI.

the non-adaptive C-CASSI. The second aspect is the optical light efficiency. In this respect, the non-adaptive C-CASSI uses an optical efficiency of 50%, while the proposed method exhibits two different transmittances that depend on the number of shots. The transmittance function for local minimum region is $\eta_u[\ell] = 1/(\ell + 1)$, and the transmittance for local maximum region is $\eta_d[\ell] = 2/(\ell + 3)$, which are smaller than 50% for $\ell > 2$. In terms of throughput of the system, the adaptive C-CASSI is less light efficient than non-adaptive C-CASSI due to the lower transmittance. However, adaptive C-CASSI overcomes the quality of image reconstruction of non-adaptive C-CASSI using less light. The third aspect is the robustness to noise. The proposed adaptive system tolerates the Gaussian noise better than non-adaptive C-CASSI. The simulations and experimental results show that non-adaptive C-CASSI is less robust to noise than adaptive C-CASSI.

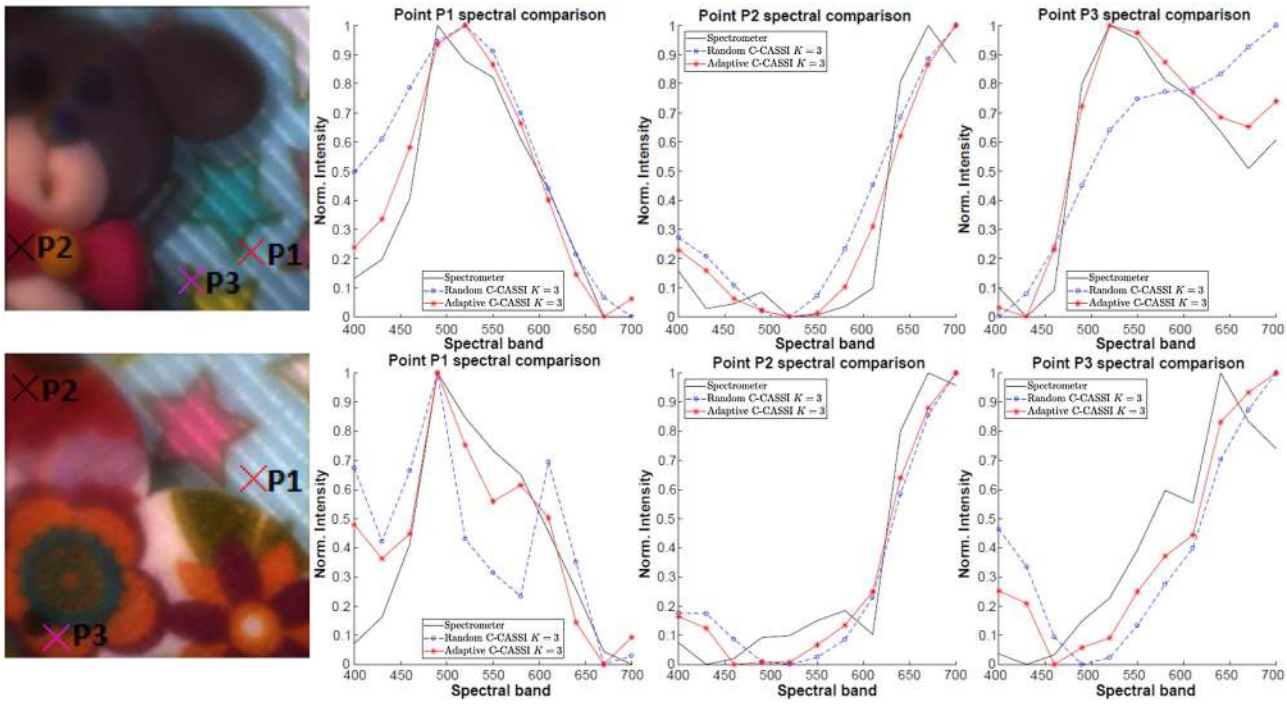

Fig. 14. Spectral signatures for three different spatial points in the target scenes, using $K = 3$. (Top row, column 1) three spatial points in the bear-stars scene. (Top row, column 2) **P1** point in the light-blue background. (Top row, column 3) **P2** point in the red bow tie. (Top row, column 4) **P3** point in the yellow star. (Bottom row, column 1) selection of the three spatial points in the flower-stars scene. (Bottom row, column 2) **P1** point in the light-blue background. (Bottom row, column 3) **P2** point in the dark-red flower petal. (Bottom row, column 4) **P3** point in the orange flower petal.

The tolerance to noise is due to the steps 4–7 of the GTA algorithm, which not only enhance spectral edges but reduce the noise. The fourth aspect of the designed adaptive CCA is dealing with the interspersion problem. The interspersion problem of traditional CASSI consists of an increase of the spatial-spectral overlap at the detector when the number of spectral bands increases; then it entails a nearly intractable reconstruction problem. The adaptively designed CCA alleviates the interspersion problem since the spectral filtering entailed by the CCA reduces the overlap, or multiplexing, per pixel in the detector.

6. CONCLUSIONS

This paper has shown the benefits of the adaptive design of a color coded aperture in C-CASSI. In particular, the coding design of the CCA adaptively promotes the spectral borders of the scene, and the resulting CCA is adjusted to the scene. The simulations and experimental implementation show the feasibility of an adaptive C-CASSI system as an alternative to non-adaptive C-CASSI with the advantage of improved quality in image reconstruction. Our proposed architecture takes advantage of the previous compressive measurements and sensing matrix to compute the following coded aperture relying on a low-resolution reconstruction data. The key feature of adaptive C-CASSI is the subsequent design of the coded apertures in relation to the spectral edges of the low-resolution data cube. The results of this study imply that the designed coded apertures not only improve the quality of image reconstruction but deal better with Gaussian noise. The simulations and numerical analysis support the idea that the proposed approach outperforms the traditional method by up to 3 dB when the measurements are contaminated with a noise of SNR $= 10$ dB. In addition, experimental reconstructions evidence the improvement of the proposed adaptive color coded aperture in comparison with the traditional non-adaptive colored random apertures.

Funding. Departamento Administrativo de Ciencia, Tecnología e Innovación (COLCIENCIAS) (727); Universidad Industrial de Santander (UIS) (2345).

Acknowledgment. Nelson Diaz and Hoover Rueda are supported by Colciencias and Fulbright scholarships, respectively. We thank the members of the optics lab from HDSP-UIS for their help with testbed experiments.

REFERENCES

1. F. G. France, "Advanced spectral imaging for noninvasive microanalysis of cultural heritage materials: review of application to documents in the U.S. Library of Congress," Appl. Spectrosc. **65**, 565–574 (2011).
2. N. Bedard, R. A. Schwarz, A. Hu, V. Bhattar, J. Howe, M. D. Williams, A. M. Gillenwater, R. Richards-Kortum, and T. S. Tkaczyk, "Multimodal snapshot spectral imaging for oral cancer diagnostics: a pilot study," Biomed. Opt. Express **4**, 938–949 (2013).
3. V. C. Coffey, "Hyperspectral imaging for safety and security," Opt. Photon. News **26**(10), 26–33 (2015).
4. R. G. Sellar and G. D. Boreman, "Classification of imaging spectrometers for remote sensing applications," Opt. Eng. **44**, 013602 (2005).
5. R. G. Sellar and G. D. Boreman, "Comparison of relative signal-to-noise ratios of different classes of imaging spectrometer," Appl. Opt. **44**, 1614–1624 (2005).
6. T. Okamoto and I. Yamaguchi, "Simultaneous acquisition of spectral image information," Opt. Lett. **16**, 1277–1279 (1991).
7. J. Stoffels, A. Bluekens, and J. Petrus, "Color splitting prism assembly," U.S. patent 4,084,180 (11 April 1978).
8. M. W. Kudenov and E. L. Dereniak, "Compact real-time birefringent imaging spectrometer," Opt. Express **20**, 17973–17986 (2012).
9. A. Wagadarikar, R. John, R. Willett, and D. Brady, "Single disperser design for coded aperture snapshot spectral imaging," Appl. Opt. **47**, B44–B51 (2008).
10. Y. Wu, I. O. Mirza, G. R. Arce, and D. W. Prather, "Development of a digital-micromirror-device-based multishot snapshot spectral imaging system," Opt. Lett. **36**, 2692–2694 (2011).
11. H. Arguello and G. R. Arce, "Rank minimization code aperture design for spectrally selective compressive imaging," IEEE Trans. Image Process. **22**, 941–954 (2013).
12. G. R. Arce, D. J. Brady, L. Carin, H. Arguello, and D. S. Kittle, "Compressive coded aperture spectral imaging: an introduction," IEEE Signal Process. Mag. **31**(1), 105–115 (2014).
13. Y. Mejia and H. Arguello, "Filtered gradient reconstruction algorithm for compressive spectral imaging," Opt. Eng. **56**, 041306 (2016).
14. H. Arguello and G. R. Arce, "Colored coded aperture design by concentration of measure in compressive spectral imaging," IEEE Trans. Image Process. **23**, 1896–1908 (2014).
15. H. Rueda, H. Arguello, and G. R. Arce, "DMD-based implementation of patterned optical filter arrays for compressive spectral imaging," J. Opt. Soc. Am. A **32**, 80–89 (2015).
16. C. Hinojosa, C. Correa, H. Arguello, and G. R. Arce, "Compressive spectral imaging using multiple snapshot colored-mosaic detector measurements," Proc. SPIE **9870**, 987004 (2016).
17. N. Diaz, H. R. Chacon, and H. A. Fuentes, "High-dynamic range compressive spectral imaging by grayscale coded aperture adaptive filtering," Ing. Invest. **35**, 53–60 (2015).
18. M. Yang, F. de Hoog, Y. Fan, and W. Hu, "Adaptive sampling by dictionary learning for hyperspectral imaging," IEEE J. Sel. Top. Appl. Earth Obs. Remote Sens. **9**, 4501–4509 (2016).
19. A. Averbuch, S. Dekel, and S. Deutsch, "Adaptive compressed image sensing using dictionaries," SIAM J. Imaging Sci. **5**, 57–89 (2012).
20. S. Ji, Y. Xue, and L. Carin, "Bayesian compressive sensing," IEEE Trans. Signal Process. **56**, 2346–2356 (2008).
21. M. L. Malloy and R. D. Nowak, "Near-optimal adaptive compressed sensing," IEEE Trans. Inf. Theory **60**, 4001–4012 (2014).
22. L. Galvis, D. Lau, X. Ma, H. Arguello, and G. R. Arce, "Coded aperture design in compressive spectral imaging based on side information," Appl. Opt. **56**, 6332–6340 (2017).
23. J. H. Mathews and K. D. Fink, *Numerical Methods Using MATLAB*, 3rd ed. (Simon & Schuster, 1998).
24. C. V. Correa, H. Arguello, and G. R. Arce, "Spatiotemporal blue noise coded aperture design for multi-shot compressive spectral imaging," J. Opt. Soc. Am. A **33**, 2312–2322 (2016).
25. R. C. Gonzalez and R. E. Woods, *Digital Image Processing*, 3rd ed. (Prentice-Hall, Inc., 2006).
26. M. A. T. Figueiredo, R. D. Nowak, and S. J. Wright, "Gradient projection for sparse reconstruction: Application to compressed sensing and other inverse problems," IEEE J. Sel. Top. Signal Process. **1**, 586–597 (2007).
27. D. H. Foster, K. Amano, S. M. C. Nascimento, and M. J. Foster, "Frequency of metamerism in natural scenes," J. Opt. Soc. Am. A **23**, 2359–2372 (2006).
28. F. Yasuma, T. Mitsunaga, D. Iso, and S. K. Nayar, "Generalized assorted pixel camera: postcapture control of resolution, dynamic range, and spectrum," IEEE Trans. Image Process. **19**, 2241–2253 (2010).